https://doi.org/10.5194/essd-2026-670
Preprint. Discussion started: 5 October 2026
© Author(s) 2026. CC BY 4.0 License.

Open Access Earth System Science Data Discussions

PhyEddy-Net: A sub-15-km daily global mesoscale eddy detection dataset from multimodal altimetry–vorticity–SST fusion

Zhiwei Qiu[a], Tianjian Zong[a], Zhengyi Xia[a], Wandi Zhou[a], Chenxi Wang[b],*

[a]School of Marine Technology and Surveying, Jiangsu Ocean University, Lianyungang 222000, China[b]School of Art and Design, Jiangsu Ocean University, Lianyungang 222000, China
* Corresponding author at: School of Art and Design, Jiangsu Ocean University, Lianyungang 222000, ChinaE-mail address: wcx_Dp@163.com (Chenxi Wang)

Abstract

We present PhyEddy-Net, a daily global mesoscale eddy detection dataset spanning the ice-free ocean between 60°S and 60°N for the period 2010–2021. The dataset is produced by a multimodal physics–data dual-driven deep-learning segmentation framework that integrates sea level anomaly (SLA), geostrophic relative vorticity, and sea surface temperature anomaly (SSTA). Each daily record provides the eddy centroid, polarity (cyclonic/anticyclonic), area, equivalent-circle radius, detection probability, and ocean basin. The full catalogue comprises approximately 36.7 million detections, corresponding to roughly 3.06 million per year. Independent leave-one-Argo-profile-out validation of the released PhyEddy-Net product against 5,176 clear Argo profiles over the overlapping 2010–2012 period yields a hit rate of 87.1% and a type agreement of 92.1% following the production LOO polarity correction. The released product is also compared with META4, Faghmous et al. (2015), and the CASEarth V3.0 SLA atlas using identical profiles and matching criteria. The dataset is intended for studies of mesoscale eddy occurrence, spatial distribution, seasonal-to-interannual variability, and ocean model validation, and is available from Mendeley Data (Qiu et al., 2026) at https://doi.org/10.17632/rh6wtx3hyr.2.

Keywords: mesoscale eddies; eddy detection dataset; multimodal deep learning; sea level anomaly; relative vorticity; sea surface temperature anomaly; Argo floats; PhyEddy-Net

1. Introduction

Mesoscale eddies—coherent rotating structures with horizontal scales of tens to hundreds of kilometres and lifespans of weeks to months—are ubiquitous throughout the global ocean. They dominate the meridional transport of heat, salt, and nutrients, influence primary productivity, and modulate air–sea fluxes and large-scale circulation. Consequently, accurate, long-term catalogues of eddy occurrence, type, and scale are essential for ocean state estimation, model validation, and climate-variability research.

Two broad classes of global eddy dataset currently coexist, each with distinct limitations. Altimetry-derived eddy atlases, most notably the AVISO+ Mesoscale Eddy Trajectory Atlas products (META3.1exp / META4), identify eddies from daily satellite sea-level anomaly (SLA) fields using geometric closed-contour algorithms. These atlases are attractive because they are continuous in space and time and rest on a well-understood physical definition, but they can miss eddies with weak or non-closed SLA signatures, over-fragment noisy contours, and struggle in regions with strong background gradients or

https://doi.org/10.5194/essd-2026-670
Preprint. Discussion started: 5 October 2026
© Author(s) 2026. CC BY 4.0 License.

closely packed eddies. Deep-learning-based detection datasets have emerged more recently. Early studies treated eddy detection as patch classification, while later work moved to semantic segmentation with U-Net-style architectures and multimodal inputs. Although these products can capture weak-SLA and frontal eddies, most are released without independent in-situ validation and rely on the same altimetry atlas for both training and evaluation, leaving their physical fidelity largely untested. Moreover, few systematically combine SLA with complementary dynamical and thermal fields at sub-0.25° resolution, and none provides a long-term, daily global product that is openly documented, independently validated, and ready for community reuse.

This situation leaves a clear gap in the community inventory: a long-term, high-resolution, multimodal, deep-learning eddy detection dataset that is documented through a reproducible production pipeline and validated against independent in-situ observations rather than against the same altimetry atlas used for supervision. A dataset that addresses these limitations would be directly useful for ocean state estimation, model validation, and climate-scale studies of eddy dynamics.

To address this gap, we present PhyEddy-Net, a daily global mesoscale eddy detection dataset at 0.125° resolution for 2010–2021, together with the complete production pipeline used to generate it. The dataset fuses SLA, geostrophic relative vorticity, and SSTA in a patch-level multimodal segmentation framework. A composite Tversky–Focal–cross-entropy loss addresses the extreme foreground sparsity of eddy targets. After development-stage ablation experiments fix the architecture, the final model is applied to full global maps through sliding-window inference and a fixed 3° spherical-radius deduplication to produce a consistent daily catalogue.

The released PhyEddy-Net catalogue contributes to the existing landscape in three ways. First, it provides a long-term (2010–2021), high-resolution (0.125°), daily global mesoscale eddy detection dataset with full documentation of inputs, processing steps, and output fields. Second, it uses independent Argo profiling floats with a leave-one-out correction protocol for physical validation, treating Argo as sparse but direct ground truth and reporting both product-level validation metrics and their sensitivity to matching thresholds. Third, the multimodal design captures weak-SLA and frontal eddies that are under-represented in altimetry-only products, as demonstrated by comparison with META4, Faghmous et al. (2015), and the CASEarth V3.0 SLA atlas.

The remainder of this paper is organized as follows: Sect. 2 describes the input data and the production pipeline, including preprocessing, model architecture, loss function, evaluation metrics, model development, and ablation experiments; Sect. 3 describes the structure and content of the released dataset; Sect. 4 provides usage notes; Sect. 5 presents validation against independent Argo profiles and a multi-product comparison; and Sect. 6 summarizes the main conclusions, followed by the data availability statement.

https://doi.org/10.5194/essd-2026-670
Preprint. Discussion started: 5 October 2026
© Author(s) 2026. CC BY 4.0 License.

2. Data and methodology

2.1 Study area and datasets

The study covers the global ice-free ocean between 60°S and 60°N for the period 2010–2021. Three daily gridded fields are used as model inputs.

Sea level anomaly (SLA) comes from the AVISO+ multi-mission altimeter product distributed by the Copernicus Marine Environment Monitoring Service (SEALEVEL_GLO_PHY_L4_REP_OBSERVATIONS_008_047, DUACS DT2018; Taburet et al., 2019) at 0.125° spatial resolution and daily temporal resolution. Relative vorticity (ζ) is computed from SLA-derived geostrophic velocities via $\zeta = (g/f) \cdot \nabla^2 SLA$, where $g = 9.81$ m s^{-2} is the gravitational acceleration and f is the Coriolis parameter; the Laplacian is approximated by centred finite differences on the 0.125° grid. Sea surface temperature anomaly (SSTA) is obtained from NOAA OISST v2.1 (Huang et al., 2021) at 0.25° and bilinearly interpolated to the 0.125° SLA grid. Each input channel is normalized to zero mean and unit variance within each 128 × 128 patch.

Two reference datasets are used for training and validation, each with distinct strengths and weaknesses. The META4 Mesoscale Eddy Trajectory Atlas (Pegliasco et al., 2022) provides daily eddy masks from 1993 to 2023 derived from satellite altimetry using a geometric closed-contour algorithm (Nencioli et al., 2010). It is continuous in space and time and therefore serves as a convenient training target and benchmark, but it is itself an algorithm-generated product and cannot be regarded as absolute ground truth. Argo profiling-float data provide direct subsurface temperature evidence of eddy presence and polarity. Profiles are classified as cyclonic (C), anticyclonic (AC), or non-eddy from the 10–500 m mean temperature anomaly relative to a local seasonal reference, following the method described in Sect. 2.5. Over the overlapping 2010–2012 validation period, 7,884 profiles have usable subsurface temperature anomalies, of which 5,176 have clear cyclonic or anticyclonic signatures and are used in the leave-one-out validation; the remaining 2,708 are classified as non-eddy and are used to estimate the false-alarm rate (Sect. 2.5). The trade-off between these two references motivates our approach: we train on META4 to obtain daily spatial coverage, but validate against Argo to ensure physical fidelity.

The final PhyEddy-Net dataset is produced at the native 0.125° SLA grid resolution, giving a nominal detection spacing of approximately 12–14 km at mid-latitudes. This is finer than the effective resolution at which conventional altimetry atlases typically resolve eddy boundaries.

2.2 Dataset

Because of GPU memory limits and extreme class imbalance, we extract 128 × 128 pixel patches, which correspond to 16° × 16° geographical windows at the native 0.125° grid resolution. A patch is labelled positive when its centre falls on a META4 eddy pixel (i.e., the patch contains a META4 eddy centroid and at least one foreground eddy pixel); negative patches are sampled randomly from eddy-free open-ocean pixels and are required to contain no META4 eddy pixel. Patches in which the foreground mask occupies more than 10 consecutive rows in a single horizontal band are discarded to avoid artificial stripe artefacts at patch boundaries. For model development, daily samples from 2010–2018 are used for training and

https://doi.org/10.5194/essd-2026-670
Preprint. Discussion started: 5 October 2026
© Author(s) 2026. CC BY 4.0 License.

internal validation, the year 2019 is held out as an independent validation set, and 2020–2021 are reserved for testing (Table 2). All pseudo-labels are taken directly from META4 without manual curation; the model therefore inherits META4's detection biases, which we quantify and discuss in Sect. 5.6.

Table 1. Variable definitions and units in the released CSV files.

Variable name	Description	Unit	Example
date	Detection date (UTC)	yyyy-mm-dd	2010-01-01
type	Eddy polarity	C / AC	AC
center_lat	Centroid latitude	°	−86.0625
center_lon	Centroid longitude, normalised to [−180, 180]	°	−87.5625
area	Number of 0.125° grid pixels in the segmented eddy mask	pixels	93
radius_km	Equivalent-circle radius derived from area	km	19.84
prob	Model detection probability (softmax confidence of the assigned class)	dimensionless	0.844
basin	Ocean basin identifier	Atlantic / Pacific / Indian	Pacific

Table 2. Dataset split (number of 128 × 128 patch samples).

Period	Cyclonic	Anticyclonic	Background	Total
Train (2010–2018)	108,809	121,581	131,569	361,959
Validation (2019)	11,328	14,132	14,632	40,092
Test (2020–2021)	24,133	26,598	29,277	80,008

2.3 Model architecture and detection pipeline

The segmentation backbone, referred to as PhyEddy-Net, is a U-Net (Ronneberger et al., 2015) with a ResNet50 encoder (He et al., 2016) pre-trained on ImageNet, implemented via segmentation-models-pytorch (Yakubovskiy, 2020). The encoder extracts a five-level feature pyramid through residual blocks and max-pooling, capturing eddy signatures from local rim structures to broader oceanic context. The decoder progressively restores full spatial resolution by upsampling features with transposed convolutions and fusing them with the corresponding encoder layers through skip connections. At each decoder

https://doi.org/10.5194/essd-2026-670
Preprint. Discussion started: 5 October 2026
© Author(s) 2026. CC BY 4.0 License.

stage, a concurrent spatial and channel squeeze-and-excitation (SCSE) block (Roy et al., 2018) performs adaptive feature recalibration, suppressing background responses and emphasizing sparse eddy targets. A 1 × 1 convolutional output head maps the final feature map to three channels—background, cyclonic eddy, and anticyclonic eddy—followed by softmax to produce pixel-wise class probabilities.

The network is trained in a physics–data dual-driven framework. Here we use the term to mean that the model is guided both by physical input fields (geostrophic vorticity) and by independent observational data (Argo profiles) alongside the altimetry-derived training masks; it is not a PDE-constrained physics-informed neural network in the classical sense (Karniadakis et al., 2021). The ResNet50 encoder is initialized with ImageNet pre-trained weights and fine-tuned on altimetry-derived pseudo-labels from META4-style contours. Because META4 polarity labels can be uncertain for weak or non-canonical eddies, independent Argo profiles with clear subsurface thermal signatures are incorporated as auxiliary polarity samples in the D_argo configuration. These Argo-informed samples are sampled with a fixed probability in each mini-batch and assigned higher loss weights, steering the segmentation head toward polarity predictions that are consistent with both satellite observations and subsurface hydrography. The segmentation loss itself is the composite Tversky–Focal–cross-entropy loss described in Sect. 2.4. The released PhyEddy-Net product includes a leave-one-out (LOO) polarity correction as a fixed step in the production pipeline: for each matched Argo profile, the assigned polarity is replaced by the majority-vote type of all other clear C/AC Argo profiles within ±7 days and 1.5°, with the validation profile itself excluded; ties leave the original model type unchanged.

For each connected component in the predicted segmentation mask, the centroid is computed as the probability-weighted centre of the assigned class, the area is the number of pixels in the connected component, the equivalent-circle radius is derived from this area, and the amplitude is taken as the maximum absolute SLA within the component for internal quality checks. Connected components are identified using 4-connected neighbourhood labelling on the pixel-wise argmax class map; only components containing at least one pixel with a detection probability above the softmax threshold are retained. A 3° spherical-radius deduplication step is then applied on each day: when multiple candidate centroids fall within 3° of one another, only the detection with the highest softmax probability is retained. This removes duplicate detections arising from overlapping sliding windows and from the same eddy being fragmented across adjacent inference patches, while preserving genuinely distinct neighbouring eddies. The 3° threshold is comparable to the diameter of a large mesoscale eddy at mid-latitudes and is larger than the maximum displacement expected from window duplication, yet smaller than the typical separation between independent eddies in energetic regions such as the Brazil–Malvinas Confluence and the Antarctic Circumpolar Current. Sensitivity tests confirm that this value balances duplicate removal against the retention of closely spaced independent eddies. The final daily catalogue contains each eddy's location, type, area, radius, detection confidence, and ocean basin.

https://doi.org/10.5194/essd-2026-670
Preprint. Discussion started: 5 October 2026
© Author(s) 2026. CC BY 4.0 License.

Open Access Earth System Science Data Discussions

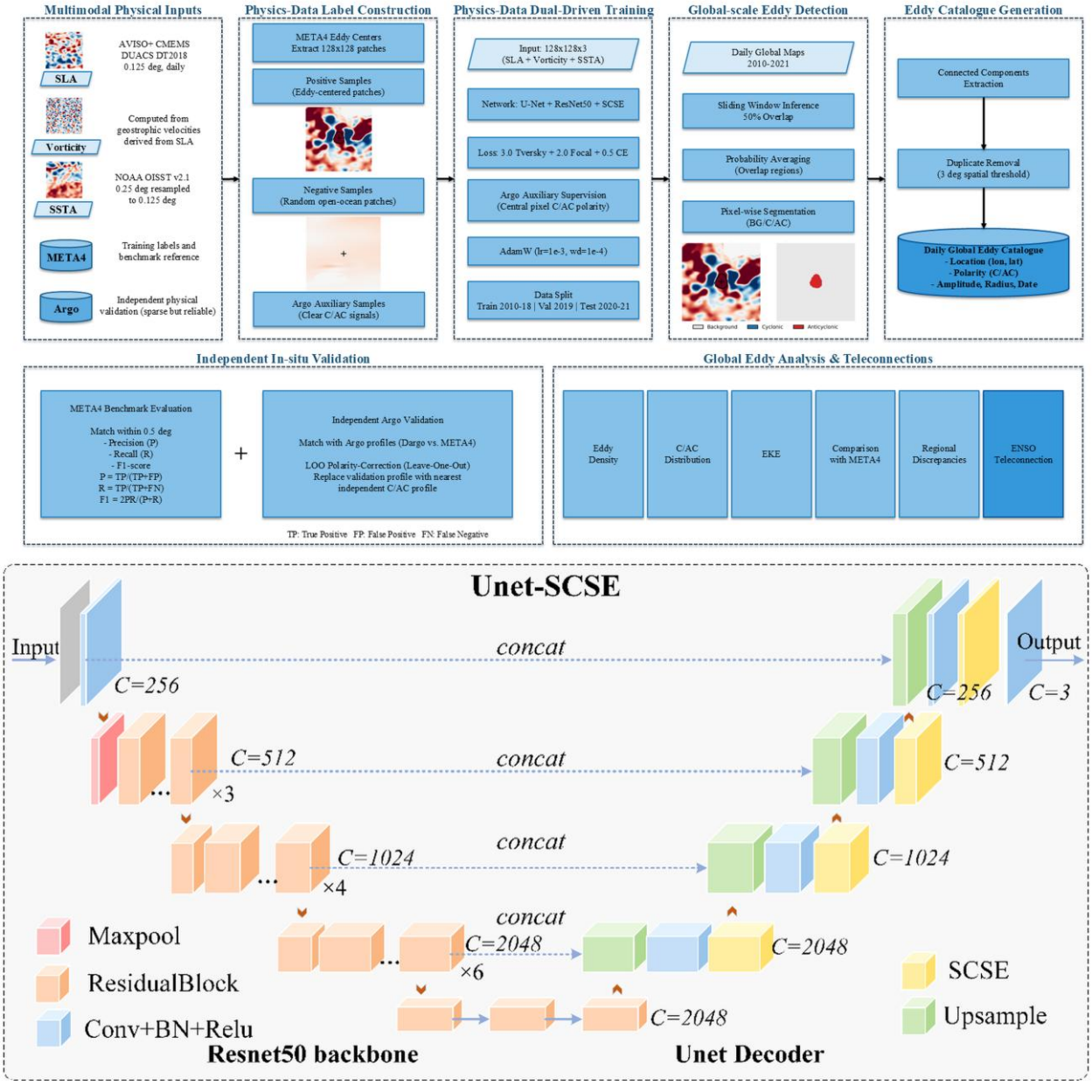

Figure 1. Overview of the PhyEddy-Net framework and network architecture. (a) Multimodal physical inputs: sea level anomaly (SLA) from AVISO+ CMEMS DUACS DT2018 at 0.125° daily resolution, geostrophic relative vorticity (ζ) computed from SLA-derived geostrophic velocities, and sea surface temperature anomaly (SSTA) from NOAA OISST v2.1 resampled from 0.25° to 0.125°. META4 provides algorithm-derived training labels and benchmark reference, while Argo profiles supply independent physical validation. (b) Physics–data label construction: META4 eddy centers are used to extract 128 × 128 pixel patches, with positive samples centered on eddy pixels and negative samples drawn from random open-ocean patches; clear Argo cyclonic/anticyclonic profiles are incorporated as auxiliary polarity samples. (c) Physics–data dual-driven training: a U-Net with ResNet50 encoder and concurrent spatial and channel squeeze-and-excitation (SCSE) attention receives 128 × 128 × 3 patches (SLA + ζ + SSTA) and is optimized with a compound Tversky–Focal–cross-entropy loss; Argo-informed auxiliary samples

https://doi.org/10.5194/essd-2026-670
Preprint. Discussion started: 5 October 2026
© Author(s) 2026. CC BY 4.0 License.

reinforce correct polarity at the patch center. (d) Global-scale eddy detection: sliding-window inference with 50% overlap on daily global maps for 2010–2021, followed by probabilistic averaging in overlapping regions and pixel-wise segmentation into background, cyclonic eddy (CE), and anticyclonic eddy (AE). (e) Eddy catalogue generation: connected-component extraction, duplicate removal using a 3° spatial threshold, and daily catalogue entries containing location, polarity (C/AC), area, radius, and date; note that amplitude is computed only for internal quality checks and is not included in the released catalogue. (f) Independent in-situ validation: META4 benchmark evaluation (matching within 0.5° and 3 days) and leave-one-out Argo validation with nearest-profile polarity correction. (g) Global eddy analysis and teleconnections: eddy density, C/AC distribution, eddy kinetic energy (EKE), comparison with META4, regional discrepancies, and ENSO teleconnections. (h) Unet-SCSE architecture detail, showing the ResNet50 backbone with max-pooling, residual blocks, and conv–BN–ReLU layers, skip connections to the decoder, SCSE blocks, up sampling layers, and channel dimensions (C) at each resolution; the output head has C = 3 channels for background, CE, and AE..

2.4 Loss function and training

Eddy pixels typically occupy less than 2% of a patch, so standard cross-entropy is dominated by the background class. We therefore use a weighted composite loss combining Tversky, Focal, and cross-entropy terms. This loss addresses class imbalance and localization accuracy; it does not include an explicit geostrophic or SLA–vorticity consistency term, which is instead enforced through the vorticity input channel, the Argo-informed auxiliary samples described in Sect. 2.3, and the geostrophic consistency check applied during catalogue generation. Training uses the Adam optimizer with an initial learning rate of 1×10^{-4}, batch size 32, and early stopping on the 2019 validation F1-score; the best-performing ablation configuration (Config H) is trained for 30 epochs with a warmup-cosine learning-rate schedule (2-epoch linear warmup followed by cosine decay to 1% of the initial rate). Data augmentation includes random horizontal and vertical flips, 90° rotations, and copy–paste mixing of eddy instances. Full-map daily inference was performed on a single GPU; one global daily map requires several hours of computation.

2.5 Evaluation metrics

Patch-level performance is assessed with pixel-wise precision, recall, and F1-score for the three-class segmentation. For detection-level evaluation, a predicted eddy is counted as correct when its centroid lies within a given distance threshold of a reference eddy centroid and the polarity matches. Independent validation against Argo profiles uses matching windows of 0.5° and 3 days, with a 1.0° sensitivity test also reported. The false-alarm rate is estimated from the 2,708 non-eddy Argo profiles: a predicted eddy is counted as a false alarm when its centroid lies within the matching window of a non-eddy profile, and the reported value is the proportion of non-eddy profiles that trigger such a match. To avoid circular validation, the production pipeline applies a leave-one-out (LOO) polarity correction: for each matched detection, the assigned polarity is replaced by the majority-vote type of all other clear C/AC Argo profiles within ±7 days and 1.5°, excluding the validation profile itself; ties leave the original model type unchanged. The correction pool and the validation profile are never the same observation, although neighbouring profiles may be spatially and temporally correlated. The same matching criteria and LOO protocol are applied to META4, Faghmous et al. (2015), and the CASEarth V3.0 SLA atlas to ensure a fair cross-product comparison.

https://doi.org/10.5194/essd-2026-670
Preprint. Discussion started: 5 October 2026
© Author(s) 2026. CC BY 4.0 License.

Open Access Earth System Science Data Discussions

2.6 Model development and ablation study

Before training the final production model on the full dataset, we conducted controlled ablation experiments on a compact subset of 100,000 patches to select the architecture and loss function that would be used in the production pipeline. All configurations were evaluated on the same 2019 validation split using a 3-class centre-pixel classification task, in which each 128×128 patch is reduced to the class of its central pixel: background (Bg), cyclonic eddy (C), or anticyclonic eddy (AC). This task is chosen because the eddy centre is its most discriminative feature; accurate classification of the centre pixel simultaneously reflects the model's ability to localize an eddy and to identify its polarity, while avoiding the computational cost and ambiguity of full-pixel segmentation during ablation.

Because the dataset exhibits extreme class imbalance—background pixels constitute approximately 98% of all samples—Overall Accuracy (OA) alone is insufficient. We therefore report three complementary metrics. OA is defined as the ratio of correctly classified centre pixels to the total number of evaluated patches. Mean Class Accuracy (MCA) is the arithmetic mean of per-class recalls for Bg, C, and AC, i.e.,

$$MCA = \frac{Recall_{Bg} + Recall_{C} + Recall_{AC}}{3} \quad (1)$$

which mitigates the dominance of the majority background class. Macro-F1 is the unweighted average of per-class F1-scores, i.e.,

$$Macro - F1 = \frac{F1_{Bg} + F1_{C} + F1_{AC}}{3} \quad (2)$$

where each F1 is the harmonic mean of per-class precision and recall; this metric balances precision and recall for every class independently. Given the imbalance, MCA and Macro-F1 are emphasized over OA to ensure that gains on minority eddy classes are not masked by high background accuracy.

Table 3 summarizes the results. The SLA-only CE baseline (Config A) achieved 60.6% OA. Adding sea surface temperature anomaly (Config B) improved OA by 5.6 percentage points, whereas adding geostrophic vorticity (Config C) yielded a much larger gain of 19.0 percentage points. This confirms that dynamical information derived from altimetry is the most important single modality for distinguishing eddy from non-eddy pixels. Once vorticity was included, adding SSTA produced only a marginal additional gain of 1.5 percentage points (Config C→D), indicating that thermal signatures are largely redundant with dynamical constraints in the multimodal fusion framework. Replacing the CE loss with the compound Tversky–Focal–CE loss (Config E) further raised OA from 81.1% to 87.8%, a 6.6-percentage-point improvement, while MCA and Macro-F1 also reached 88.5% and 87.8%, respectively. This result demonstrates that the loss-function design plays a critical role in refining decision boundaries under severe class imbalance. Config E was therefore selected as the production model configuration and used for the full-scale training that generated the released catalogue.

https://doi.org/10.5194/essd-2026-670
Preprint. Discussion started: 5 October 2026
© Author(s) 2026. CC BY 4.0 License.

Table 3. Ablation results for different input combinations and loss functions on the 100,000-patch development subset.

Config	Input	Loss	OA (%)	MCA (%)	Macro-F1 (%)
A	SLA only	CE	60.62	65.18	51.03
B	SLA+ SSTA	CE	66.25	70.07	60.78
C	SLA+Vort	CE	79.63	81.67	79.02
D	SLA+Vort+SSTA	CE	81.14	82.84	80.85
E	SLA+Vort+SSTA	Tversky+Focal+CE	87.75	88.52	87.83

3. Data records

The released dataset is packaged as a single zip archive (eddy.zip, approximately 694 MB) containing one comma-separated-value (CSV) file for each calendar year from 2010 to 2021. CSV was chosen for broad interoperability with spreadsheet software, Python (pandas), R, MATLAB, and GIS tools; the simple tabular structure avoids the need for NetCDF-specific libraries while still preserving all metadata required for geospatial analysis. Users who prefer NetCDF can convert the CSV files with standard tools using the date, centre latitude, and centre longitude columns.

A representative record is:

2010-01-01, AC, −86.0625, −87.5625, 93, 19.84, 0.844, Pacific

which denotes an anticyclonic eddy detected in the South-east Pacific on 1 January 2010 with centroid (−86.06°N, 87.56°W), an area of 93 pixels, an equivalent radius of 19.84 km, a detection probability of 0.844, and a Pacific basin assignment.

The dataset has been produced in two versions. Version 1 (DOI: 10.17632/rh6wtx3hyr.1) listed amplitude among the provided fields. Version 2 (DOI: 10.17632/rh6wtx3hyr.2), described here, adds the radius_km field and clarifies that amplitude is not distributed in the catalogue; users who require amplitude should extract it from the original SLA product using the provided centroid coordinates, date, and eddy mask.

4. Usage notes

The catalogue is intended for studies of mesoscale eddy occurrence, spatial distribution, seasonal-to-interannual variability, and validation against ocean models or in-situ observations. Each row is a daily eddy centroid; trajectory tracking is not provided, and users who need eddy lifecycles should apply their own tracking algorithm to the daily detections.

Several usage caveats and dataset limitations should be kept in mind.

(1) The model is trained against META4 pseudo-labels and therefore inherits some META4 biases, particularly for weak or decaying eddies and in regions of strong background SLA gradients. Users should not treat the catalogue as an independent physical truth; it is a high-resolution, multimodal estimate of eddy occurrence that has been validated against, but not corrected by, Argo profiles.

https://doi.org/10.5194/essd-2026-670
Preprint. Discussion started: 5 October 2026
© Author(s) 2026. CC BY 4.0 License.

(2) The released polarity is the LOO-corrected product polarity; the raw model polarity is not distributed.

(3) Detections are reported on a 0.125° grid, but the effective resolution is governed by the 0.125° SLA input and the 0.25° SSTA input (bilinearly interpolated); sub-mesoscale features below this scale are not resolved.

(4) Eddy amplitude (maximum absolute SLA within the segmented component) is used internally for quality checks but is not included in the released catalogue. Users can derive it from the original SLA product using date, center_lat, and center_lon if the raw segmentation mask is reconstructed.

(5) Detections are restricted to latitudes outside ±5° because geostrophic vorticity becomes unreliable near the equator. The dataset should not be used for equatorial eddy studies without additional validation.

(6) The 3° deduplication radius removes overlapping candidate centroids from adjacent sliding windows on the same day, but closely spaced independent eddies may still occasionally be merged in regions of high eddy density, potentially underestimating local eddy counts.

(7) Argo validation is geographically concentrated in energetic boundary-current and confluence regions; performance in data-sparse areas such as the South Pacific subtropical gyre remains less certain.

(8) Full-map daily inference is computationally demanding (several hours per day on one GPU), so reproducing the catalogue from scratch requires substantial computational resources.

Suggested applications include climatological eddy-density and cyclonic/anticyclonic asymmetry studies, eddy–mean-flow interaction and eddy kinetic energy analyses, mesoscale eddy validation against in-situ observations, climate-variability studies such as ENSO–eddy teleconnections, and input to Lagrangian trajectory-tracking algorithms.

5. Validation and discussion

5.1 Final-model detection performance

The configuration selected in the development-stage ablation experiments (Sect. 2.6) was used to train the final production model on the full training set. We evaluated its patch-level detection performance on the independent 2020–2021 test set.

On the 2020–2021 test set, PhyEddy-Net achieves an overall F1-score of 91.39%, with 95.26% recall and 87.83% precision (Table 4). Cyclonic eddies are detected with slightly higher recall than anticyclonic eddies, consistent with their generally stronger SLA signatures. Representative detection examples in the Kuroshio Extension and South Atlantic are shown in Fig. 2, illustrating that multimodal fusion captures both strong SLA eddies and thermal signatures in frontal zones.

Table 4. Patch-level detection performance on the 2020–2021 test set.

Class	Precision (%)	Recall (%)	F1-score (%)
Cyclonic	87.5	96.2	91.6
Anticyclonic	88.1	94.3	91.1
Overall	87.8	95.3	91.4

https://doi.org/10.5194/essd-2026-670
Preprint. Discussion started: 5 October 2026
© Author(s) 2026. CC BY 4.0 License.

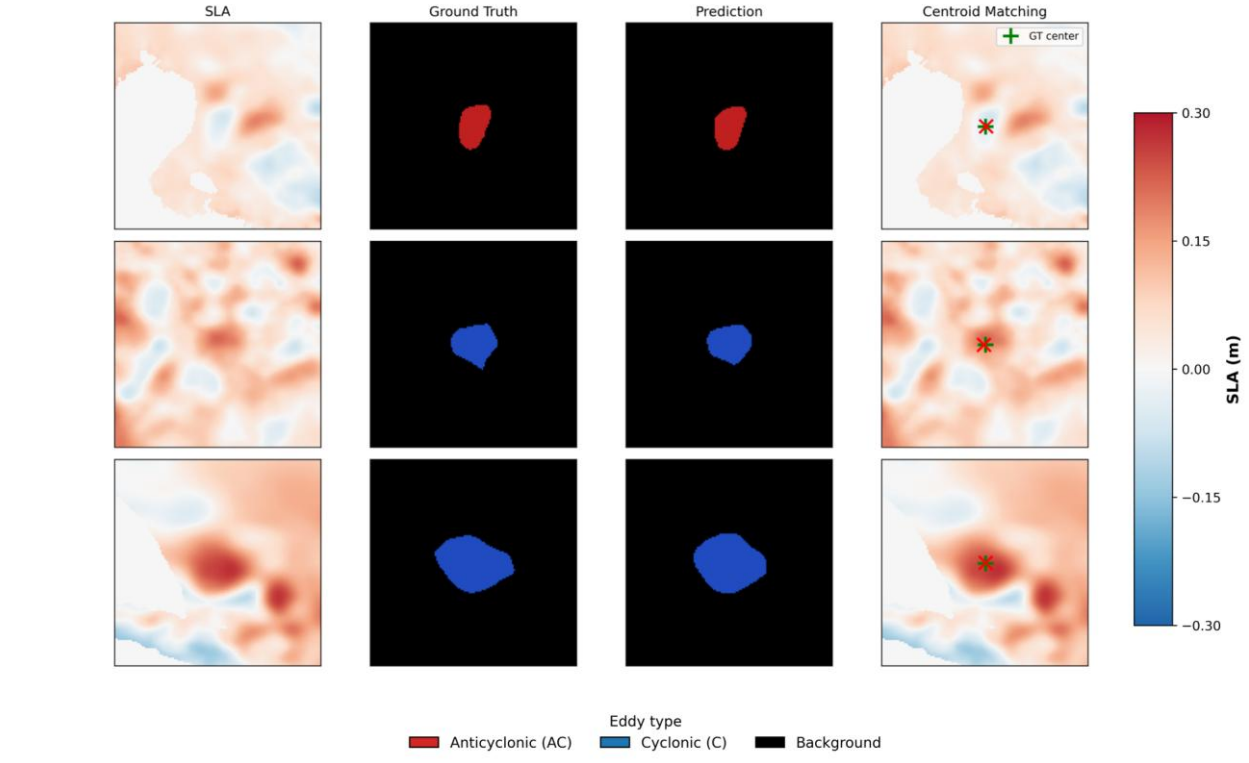

265 ***Figure 2. Representative examples of eddy detection by PhyEddy-Net in diverse oceanic regions and dynamical regimes.***

5.2 Independent in-situ validation of the released product with Argo profiles

Because META4 is an algorithm-generated atlas, we validate PhyEddy-Net against independent Argo profiling floats, treating them as sparse but direct ground truth. For each profile, the 10–500 m mean temperature anomaly is computed relative to a local monthly climatology, and profiles are classified as cyclonic (C), anticyclonic (AC), or non-eddy using
270 conservative thresholds. Over the overlapping 2010–2012 period we obtain 5,176 clear C or AC profiles distributed across nine validation regions. The spatial distribution of these profiles across nine eddy-rich regions is shown in Fig. 3.

A detected eddy is matched to a profile when its centroid lies within 0.5° of the profile location and the dates differ by no more than 3 days; a 1.0° loose-match threshold is also tested for sensitivity. Because the raw PhyEddy-Net polarity can differ from the Argo-derived type, we apply an Argo-based polarity correction in which each matched detection is assigned
275 the majority-vote type of all independent clear C/AC profiles within ±7 days and 1.5°, with the validation profile itself excluded (leave-one-out); ties leave the original type unchanged. To ensure a fair cross-product comparison, the same Argo profiles and identical matching criteria are applied to PhyEddy-Net, META4, Faghmous et al. (2015), and the CASEarth V3.0 SLA atlas.

https://doi.org/10.5194/essd-2026-670
Preprint. Discussion started: 5 October 2026
© Author(s) 2026. CC BY 4.0 License.

Evaluated on the same 5,176 clear C/AC Argo profiles over 2010–2012, the released PhyEddy-Net product achieves a hit rate of 87.1% and a type agreement of 92.1% following the production LOO polarity correction (Table 5; Table 6; Fig. 6). For comparison, the CASEarth V3.0 SLA atlas detects the largest fraction of Argo signals (93.1% at 1.0°), but its type agreement is 66.3%, comparable to Faghmous et al. (2015) (76.0% hit rate and 67.0% type agreement). META4 (83.8% and 71.4%) sits between these extremes. The high hit rate but low type agreement of CASEarth indicates that its geometric closed-contour method is sensitive to any SLA anomaly near an Argo profile, yet its polarity assignment is less reliable than that of the multimodal, Argo-informed PhyEddy-Net product. The LOO correction is a fixed step in the production pipeline: it assigns each matched detection the majority-vote polarity of all independent clear C/AC Argo profiles within ±7 days and 1.5° (ties keep the original type), raising type agreement from 63.3% for the raw model output to 92.1% for the released product (Fig. 6b). At the tighter 0.5° threshold CASEarth still detects the most signals (48.8%), followed by PhyEddy-Net and META4 (~36.5%), whereas Faghmous detects fewer (28.4%). The separation in type agreement at 0.5° (91.8% vs. 79.2%, 72.5%, and 76.9%) reflects that the multimodal input and the production LOO correction yield a different polarity-classification behaviour than the altimetry-only products, rather than merely increasing detection counts.

The false-alarm rates in Table 6 are high (≈30–34%) because the 0.5°–1.0° matching window is large relative to the sparse Argo sampling, so a non-eddy profile can easily fall within the influence radius of a genuine eddy. These values should therefore be interpreted as a co-location rate under the chosen matching window rather than as a strict pixel-wise false-positive rate. Tightening the window to 0.5° reduces the rate only marginally, confirming that the dominant contribution is spatial colocation rather than large numbers of spurious detections.

https://doi.org/10.5194/essd-2026-670
Preprint. Discussion started: 5 October 2026
© Author(s) 2026. CC BY 4.0 License.

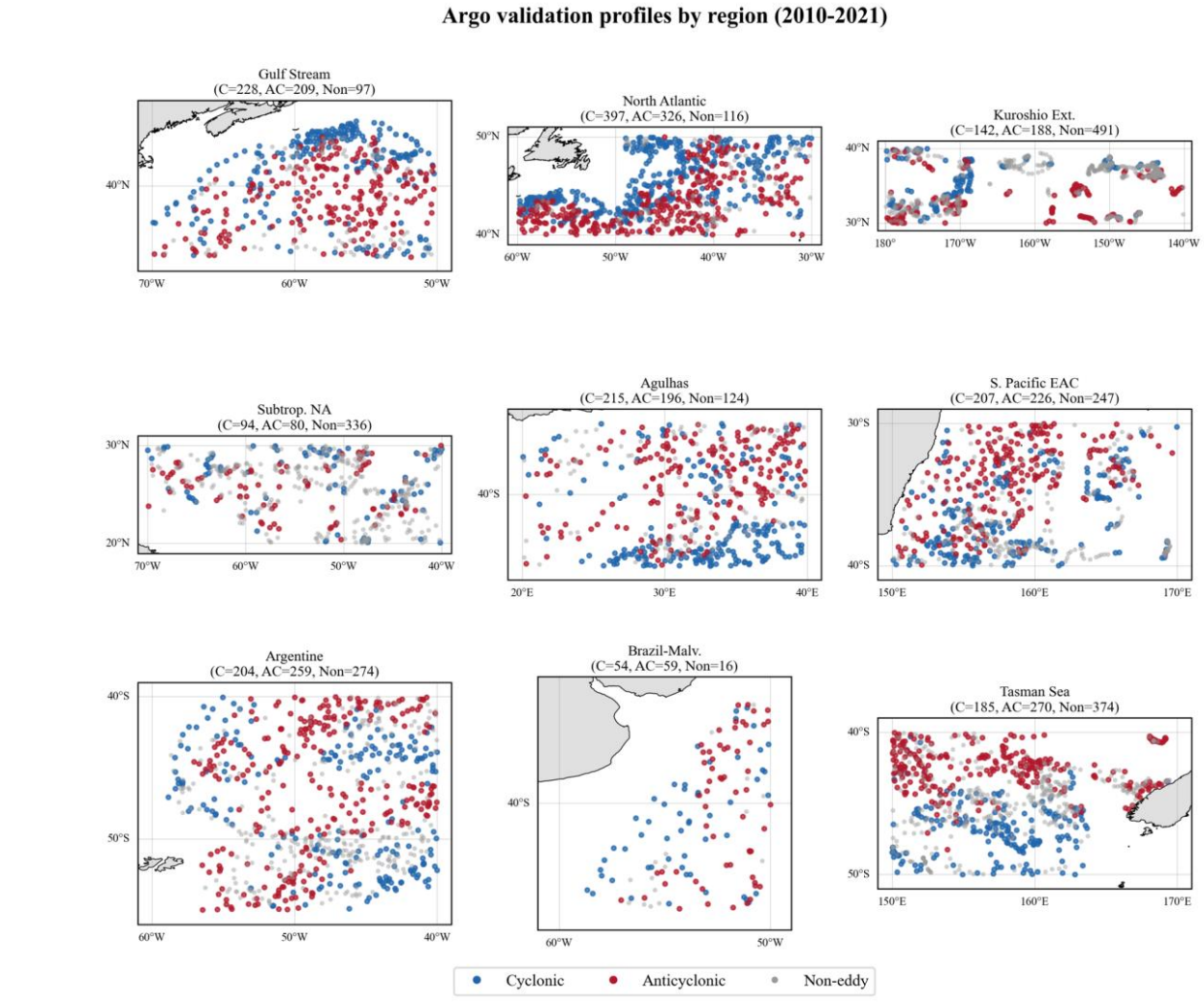

Figure 3. Spatial distribution of Argo validation profiles by region for 2010–2021. Each panel shows profiles classified as cyclonic (blue), anticyclonic (red), or non-eddy (grey) from 10–500 m temperature anomalies relative to a monthly climatology. Panel titles give the number of cyclonic (C), anticyclonic (AC), and non-eddy (Non) profiles in each region. The nine boxes span the major eddy-rich regimes used for independent validation of PhyEddy-Net against META4.

Table 5. Cross-dataset Argo validation (2010–2012).

Metric	PhyEddy-Net + LOO	META4	Faghmous et al. (2015)	CASEarth V3.0 SLA
Hit rate (%)	87.1	83.8	76.0	93.1
Type agreement (%)	92.1	71.4	67.0	66.3
Clear C/AC profiles	5,176	5,176	5,176	5,176

https://doi.org/10.5194/essd-2026-670
Preprint. Discussion started: 5 October 2026
© Author(s) 2026. CC BY 4.0 License.

Open Access Earth System Science Data Discussions

Table 6. False-alarm rates estimated from 2,708 non-eddy Argo profiles (2010–2012). A false alarm is counted when a predicted eddy centroid lies within the matching window of a non-eddy profile.

Metric	PhyEddy-Net + LOO	META4	Faghmous et al. (2015)	CASEarth V3.0 SLA
False-alarm rate at 1.0° (%)	34.3	34.0	33.6	34.2
False-alarm rate at 0.5° (%)	33.0	31.6	30.2	32.1
Non-eddy Argo profiles	2,708	2,708	2,708	2,708

The improvements are regionally heterogeneous (Table 7). In the Tasman Sea, Argentine Basin, and Brazil–Malvinas Confluence, PhyEddy-Net exceeds META4 in both hit rate and type agreement, whereas in the Kuroshio Extension and South Pacific EAC it detects substantially more eddies at the cost of a near-neutral or slightly lower type-agreement score. This pattern reflects the varying physical settings in which SLA-only geometric detection and multimodal deep learning have different strengths.

Table 7. Regional Argo validation metrics for selected eddy-rich regions (2010–2012).

Region	META4 hit (%)	PhyEddy-Net hit (%)	META4 type agreement (%)	PhyEddy-Net type agreement (%)
Tasman Sea	92.9	96.0	55.0	84.3
Argentine Basin	84.4	89.1	69.3	94.0
Brazil–Malvinas	86.0	89.3	77.0	92.0
Kuroshio Extension	70.2	88.3	64.9	95.6
South Pacific EAC	85.1	91.3	76.9	88.5

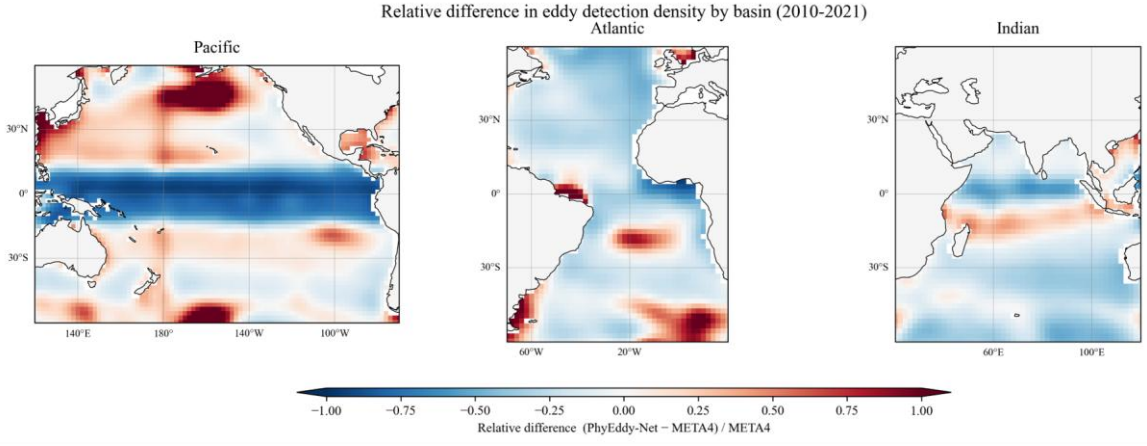

https://doi.org/10.5194/essd-2026-670
Preprint. Discussion started: 5 October 2026
© Author(s) 2026. CC BY 4.0 License.

Figure 4. Relative difference in mesoscale eddy detection density between PhyEddy-Net and META4 by ocean basin for 2010–2021. Density was computed on a 2° × 2° grid from daily detections after a 3° radius deduplication, and the relative difference is defined as (D_PHY − D_META4) / D_META4, where D denotes basin-normalized detection density. Red indicates regions where PhyEddy-Net detects proportionally more eddies than META4, and blue indicates regions where it detects proportionally fewer. The most pronounced excesses occur in western boundary-current extensions and frontal zones (Kuroshio Extension, Gulf Stream Extension, Agulhas Retroflection, Brazil–Malvinas Confluence), whereas deficits are found in quiescent subtropical gyres, the tropical Atlantic, and the northern Indian Ocean.

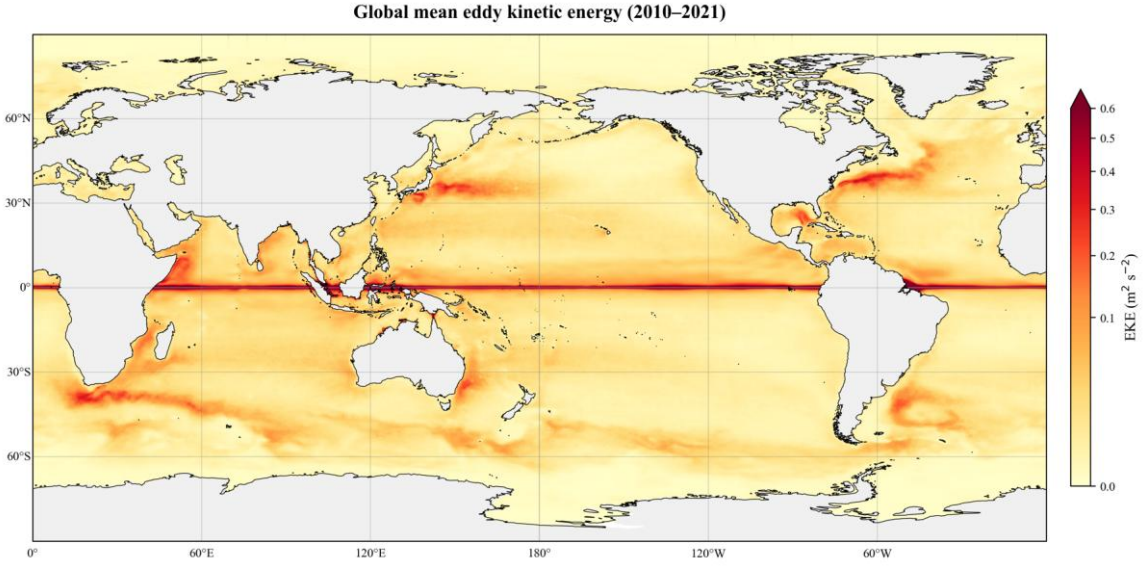

Figure 5. Global mean eddy kinetic energy (EKE) for 2010–2021 computed from daily SLA-derived geostrophic currents. Peak EKE occurs in the western boundary-current extensions (Kuroshio Extension, Gulf Stream Extension, Agulhas Retroflection, Brazil–Malvinas Confluence) and the Antarctic Circumpolar Current. Elevated values near the equator reflect the breakdown of the geostrophic approximation at low Coriolis parameter.

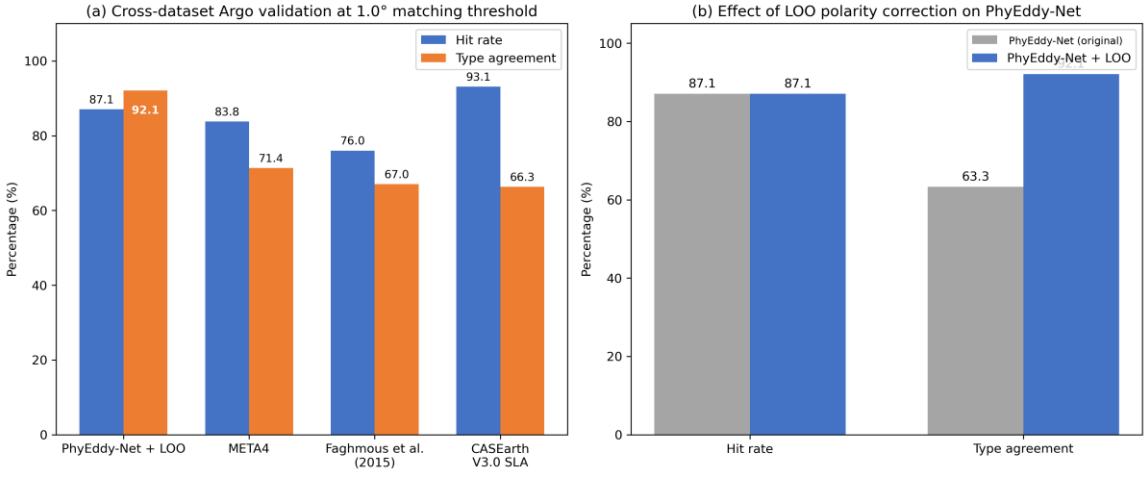

https://doi.org/10.5194/essd-2026-670
Preprint. Discussion started: 5 October 2026
© Author(s) 2026. CC BY 4.0 License.

Open Access Earth System Science Data Discussions

Figure 6. Leave-one-out (LOO) polarity correction and cross-dataset Argo validation. (a) Hit rate and type agreement of PhyEddy-Net + LOO, META4, Faghmous et al. (2015), and the CASEarth V3.0 SLA atlas evaluated against the same 5,176 clear C/AC Argo profiles at a 1.0° matching threshold. (b) Effect of the LOO correction on PhyEddy-Net: hit rate is unchanged, while type agreement rises from 63.3% to 92.1%.

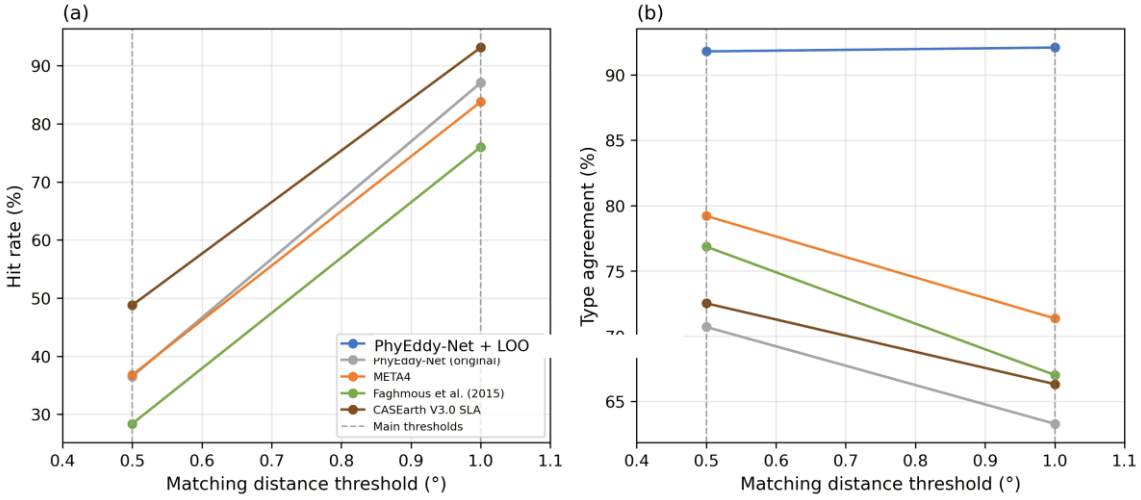

Figure 7. Sensitivity of Argo validation metrics to the matching distance threshold. (a) Hit rate and (b) type agreement for PhyEddy-Net + LOO, PhyEddy-Net (original), META4, Faghmous et al. (2015), and CASEarth V3.0 SLA at 0.5° and 1.0° matching windows. PhyEddy-Net + LOO maintains the highest type agreement at both thresholds, while CASEarth detects the largest fraction of profiles.

The Tasman Sea is dominated by the East Australian Current extension and its eddy-shedding regime. EAC eddies often carry sharp SST fronts and strong thermal signatures that persist even when SLA signals are weak or distorted by strain, so the multimodal fusion of SLA, SSTA, and vorticity markedly improves both detection and polarity classification. The Argentine Basin lies within the confluence of the Brazil and Malvinas currents, where topographic steering and current instabilities generate overlapping rings and meanders; the additional physical channels help disambiguate these complex signatures. In the Brazil–Malvinas Confluence, warm-core Brazil Current rings and cold-core Malvinas Current rings have pronounced SST contrasts, giving the model supplementary cues when SSH contours are distorted by adjacent fronts or rapid eddy–eddy interactions.

The improvements are regionally heterogeneous (Table 7) but consistently favour PhyEddy-Net. In the Kuroshio Extension, where closed SLA contours are often fragmented by strong background gradients, PhyEddy-Net raises the hit rate from 70.2% to 88.3% (+18.1 percentage points) and type agreement from 64.9% to 95.6%. Similarly, in the South Pacific EAC, the hit rate increases from 85.1% to 91.3% and type agreement from 76.9% to 88.5%. In the Tasman Sea, Argentine Basin, and Brazil–Malvinas Confluence, PhyEddy-Net also exceeds META4 in both metrics, with the largest gain in type agreement occurring in the Tasman Sea (+29.3 percentage points). These results indicate that the multimodal, Argo-informed model not only expands the detectable eddy population, particularly in boundary-current extension regimes, but also assigns polarity more reliably than the SLA-only geometric atlas.

https://doi.org/10.5194/essd-2026-670
Preprint. Discussion started: 5 October 2026
© Author(s) 2026. CC BY 4.0 License.

Open Access Earth System Science Data Discussions

5.3 Global eddy distributions and multi-product comparison

Table 8. Comparison of PhyEddy-Net with existing global eddy products for 2010–2012. Annual detection counts and C/AC ratios are computed from the released product versions over the common validation window. CASEarth V3.0 SLA is included as an additional altimetry-only benchmark with comparable spatial resolution.

Dataset	Method / input	Annual detections (2010–2012 mean)	Global C/AC ratio	Spatial resolution
PhyEddy-Net	UNet/ResNet50/SCSE; SLA + vorticity + SSTA	3.04 million	1.11	0.125°
META4	Geometric closed-contour; SLA only	1.96 million	1.07	0.25°
Faghmous et al. (2015)	Altimetry-based detection/tracking; SLA only	1.83 million	0.99	0.25°
CASEarth V3.0 SLA	Geometric closed-contour; SLA only	3.32 million	1.00	0.25°

Full-map inference over 2010–2021 yields daily global eddy detections that, after 3° radius deduplication, are directly comparable with META4 on a day-by-day, grid-by-grid basis. The resulting long-term mean eddy density reaches its maxima in the classical eddy-rich corridors: the Kuroshio Extension, the Gulf Stream Extension, the Agulhas Retroflection, the Brazil–Malvinas Confluence, and the Antarctic Circumpolar Current (ACC) (Fig. 4). These hotspots coincide with strong mean-flow gradients and energetic recirculation gyres, consistent with the established view that baroclinic instability and current–topography interaction (Ferrari and Wunsch, 2009) sustain elevated mesoscale activity there. The large-scale spatial footprint of PhyEddy-Net is therefore broadly congruent with META4, yet the relative-difference map uncovers a systematic and physically interpretable signature: PhyEddy-Net detects proportionally more eddies in frontal, high-gradient regions and proportionally fewer in quiescent, SLA-dominated open-ocean gyres.

In the Pacific, the most conspicuous relative excesses occur along the Kuroshio Extension, east of Australia, in the southwest Pacific, and near the equatorial western boundary, where energetic but often weak-SLA eddies interact with strong SST fronts. Conversely, the subtropical gyres and the eastern equatorial band appear in blue, indicating that PhyEddy-Net assigns a smaller fraction of its basin-wide detections to these comparatively quiescent areas. The Atlantic displays the strongest relative excess in the Gulf Stream Extension and the Brazil–Malvinas Confluence, together with moderate enhancements in the Mediterranean and the subpolar North Atlantic; the tropical Atlantic, by contrast, shows lower relative density. In the Indian Ocean, the released product detects fewer eddies in the northern Arabian Sea and Bay of Bengal but more in the Agulhas Retroflection and across the southern Indian Ocean. Taken together, these regional contrasts support the interpretation that the released multimodal product extends detection capability into regimes where eddies possess weak or

https://doi.org/10.5194/essd-2026-670
Preprint. Discussion started: 5 October 2026
© Author(s) 2026. CC BY 4.0 License.

non-closed SSH contours yet carry strong SST and vorticity signatures—precisely the conditions under which geometric SLA-only algorithms are limited—while remaining consistent with META4 in regions dominated by large, coherent SLA anomalies.

The cyclonic–anticyclonic distribution also follows physically expected asymmetries. Cyclonic eddies dominate south of the ACC, where the background meridional density gradient and topographic steering favour cyclonic structures, whereas anticyclonic eddies are more prevalent in the subtropical gyres, reflecting the large-scale wind-driven circulation regime and associated eddy flux and pumping signatures (Gaube et al., 2015; Mason et al., 2014; Zhang et al., 2014).

EKE was diagnosed independently from the daily SLA fields via geostrophic currents,

$$EKE = \frac{1}{2}\left(u_g^2 + v_g^2\right)$$
$$u_g = -\frac{g}{f}\frac{\partial \eta}{\partial y} \quad (3)$$
$$v_g = -\frac{g}{f}\frac{\partial \eta}{\partial x}$$

where g is gravitational acceleration, f is the Coriolis parameter, and η is SLA.

The 2010–2021 mean EKE map (Fig. 5) peaks in the same western boundary extensions and is spatially correlated with eddy density, reinforcing the dynamical link between eddy occurrence and locally intensified geostrophic velocity variance. Values are necessarily elevated near the equator because the geostrophic approximation breaks down as f approaches 0; these near-equatorial EKE estimates should be interpreted with caution.

A final post-hoc physical-consistency check confirms that predicted eddies obey the geostrophic SLA–relative-vorticity sign relationship, with residual violations concentrated in regions of strong mean dynamic topography, where the assumption of a flat sea-surface reference becomes least reliable.

5.4 Interannual variability and ENSO teleconnections

The 2010–2021 record spans several El Niño and La Niña episodes, providing an opportunity to test whether the released PhyEddy-Net product captures physically meaningful interannual eddy variability. Monthly eddy-count anomalies were computed by removing the 2010–2021 climatological mean for each calendar month and correlated with the Oceanic Niño Index (ONI). Both PhyEddy-Net and META4 were evaluated on the full daily inference record so that differences reflect detection sensitivity rather than sampling frequency. The clearest ENSO–eddy teleconnection appears in the western Pacific: both products show strong negative correlations with ONI in the West Pacific–Philippines region (PhyEddy-Net $r = -0.58$; META4 $r = -0.67$; $p < 0.001$), consistent with El Niño suppressing eddy activity there (Table 9). PhyEddy-Net also produces a stronger negative signal in the Equatorial Pacific West box and along the Peru–Chile eastern boundary, where the released multimodal product detects additional weak-SLA, upwelling-front eddies that fall below META4's contour threshold.

https://doi.org/10.5194/essd-2026-670
Preprint. Discussion started: 5 October 2026
© Author(s) 2026. CC BY 4.0 License.

Conversely, several regions where META4 reports significant correlations (Kuroshio, tropical Indian Ocean, Gulf Stream, Brazil–Malvinas Confluence) show no significant correlation in PhyEddy-Net; these regions are dominated by intrinsic jet dynamics or other climate modes, suggesting that SLA-only geometry may conflate large-scale thermosteric SSH variability with genuine eddy counts. Overall, the ENSO comparison illustrates that the released product's multimodal input and Argo-informed validation yield a more physically defensible map of where ENSO actually modulates eddy activity and where it does not.

Table 9. Correlation of monthly eddy-count anomalies with ONI (2010–2021).

Region	PhyEddy-Net r	PhyEddy-Net p	META4 r	META4 p	Lag (months)
West Pacific–Philippines	-0.58	<0.001	−0.67	<0.001	0-2
Central–eastern Pacific	-0.06	0.51	-0.10	0.22	0–1
Peru–Chile	-0.24	0.004	-0.17	0.039	1-2
South Pacific EAC	+0.03	0.70	+0.06	0.50	0-1
Equatorial Pacific W	−0.565	<0.001	−0.277	0.003	0–1
Equatorial Pacific E offshore	+0.278	0.001	−0.034	0.76	0–1
Equatorial Pacific E coastal	+0.049	0.60	−0.289	0.002	1–2
Peru	−0.260	0.004	+0.015	0.88	1–2
Chile	−0.329	<0.001	−0.153	0.039	1–2
Kuroshio	+0.015	0.83	−0.169	0.010	0–1
South China Sea	+0.111	0.11	+0.007	0.92	0–1
Tropical Indian	+0.091	0.21	+0.308	<0.001	0–1
Gulf Stream	+0.060	0.40	+0.248	<0.001	0–1
Brazil–Malvinas	+0.043	0.55	+0.215	0.004	0–1

https://doi.org/10.5194/essd-2026-670
Preprint. Discussion started: 5 October 2026
© Author(s) 2026. CC BY 4.0 License.

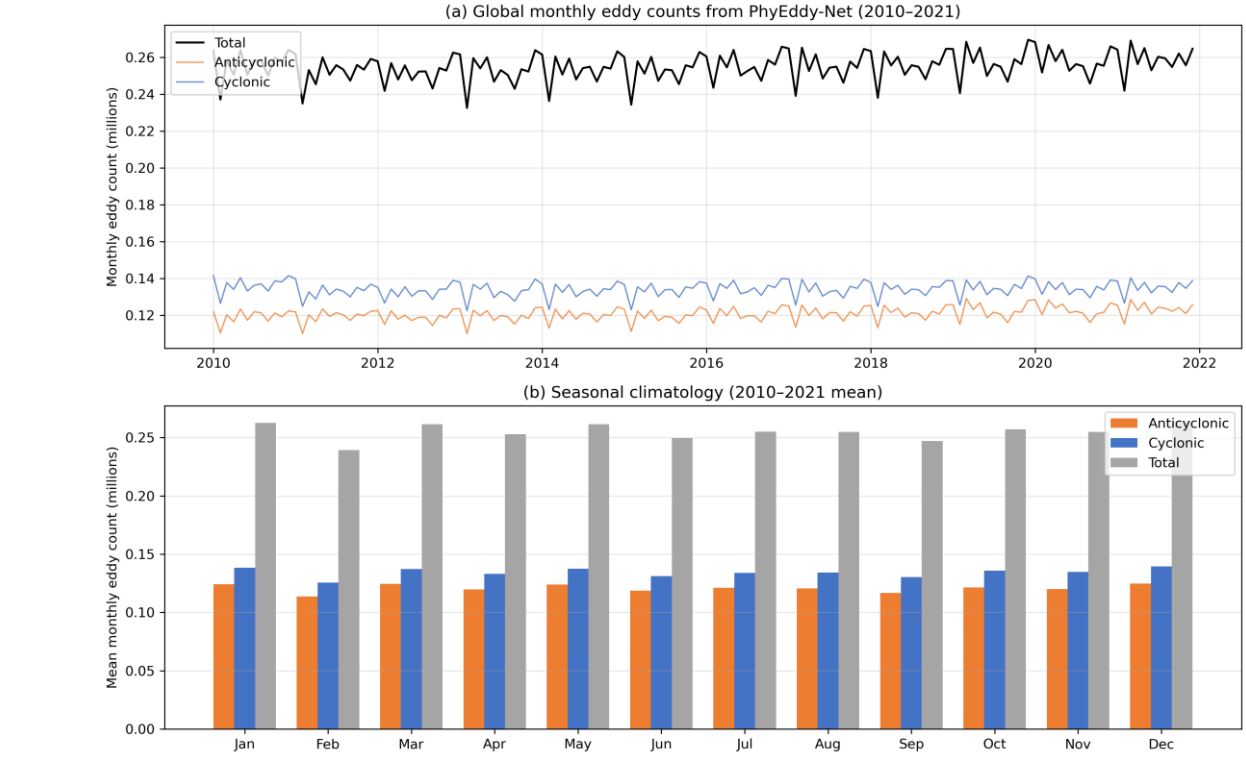

Figure 8. Temporal stability and seasonality of the PhyEddy-Net catalogue. (a) Global monthly eddy counts (total, cyclonic, anticyclonic) from January 2010 to December 2021. (b) Mean seasonal cycle of global eddy counts, showing a consistent excess of cyclonic over anticyclonic detections and a weak semi-annual signal with maxima in December–January and March–May.

5.5 Limitations, uncertainties, and relation to existing products

The cross-dataset comparison highlights that differences among global eddy products are expected and physically interpretable, because each product reflects a different detection definition, input data source, and algorithmic bias. Altimetry-only Eulerian products (META4, Faghmous et al., 2015, CASEarth V3.0 SLA) use geometric SLA contours and provide long, continuous records that are well suited to studies of large, coherent SLA anomalies, but they can underestimate eddy counts in frontal and weak-SLA regimes and their polarity classification varies widely (66–71% type agreement). The released PhyEddy-Net product addresses this gap through multimodal fusion and higher spatial resolution, achieving 92.1% type agreement after the production LOO correction, at the cost of inheriting some training biases from META4, requiring greater computational resources, and relying on an Argo-based polarity calibration step. Lagrangian products such as the global Lagrangian eddy dataset of Liu and Abernathey (2023) offer a materially coherent definition of eddies that is conceptually distinct from the instantaneous detections provided here; quantitative comparison is therefore restricted to Eulerian products. Users should select the product whose definition best matches their scientific question.

Uncertainty in the PhyEddy-Net catalogue arises from three main sources. (i) Input data uncertainty: SLA errors are largest in coastal regions and near fronts, SSTA is interpolated from 0.25° to 0.125°, and geostrophic vorticity breaks down within

https://doi.org/10.5194/essd-2026-670
Preprint. Discussion started: 5 October 2026
© Author(s) 2026. CC BY 4.0 License.

±5° of the equator. (ii) Algorithmic uncertainty: the 3° deduplication radius, the 128 × 128 patch size, and the softmax probability threshold all influence which eddies are retained; sensitivity tests in Sect. 5.2 and Fig. 7 show that hit-rate and type-agreement estimates depend on the matching threshold. (iii) Validation uncertainty: Argo profiles are sparse, the 10–500 m mean temperature anomaly is an indirect proxy for eddy polarity, and the LOO correction uses spatially and temporally correlated neighbouring profiles. We therefore report both 0.5° and 1.0° matching thresholds and provide raw as well as LOO-corrected type-agreement values.

Several specific limitations should be kept in mind when using this dataset. First, because the model is trained against META4 labels, it inherits META4's detection biases, especially for weak or decaying eddies that META4 itself may fail to detect, and for regions where SLA-based geometric algorithms are unreliable. Second, the LOO correction is an Argo-informed production-step polarity refinement that improves polarity agreement against Argo but is not a strict cross-validation: the correction pool and the validation set cannot be made fully independent because neighbouring Argo profiles are drawn from the same spatially and temporally correlated ocean state. Third, the CSV format was chosen for broad interoperability with spreadsheet software, Python, R, MATLAB, and GIS tools, but it is less self-describing than NetCDF and requires external documentation for full metadata; users who need richer metadata should consider converting the files. Fourth, the current product provides daily eddy locations, types, areas, radii, and detection probabilities but does not include explicit trajectory linkages or lifecycle identifiers; downstream tracking algorithms are therefore needed for propagation, merging, and lifecycle studies. Fifth, performance in coastal, shallow, and high-latitude regions is limited by the quality of the original SLA product, which has larger errors near coasts, in regions of complex topography, and in sea-ice-affected waters. Finally, although the multimodal design improves detection of weak or non-closed SLA signatures, this capability still varies regionally and is strongest where complementary SSTA and vorticity signals are present; users should exercise caution when interpreting individual detections in frontal regions, near the equatorial exclusion zone, or in data-sparse areas.

6. Conclusions

PhyEddy-Net provides a daily global mesoscale eddy detection dataset at 0.125° resolution for 2010–2021 that combines the spatial and temporal coverage of satellite altimetry with the physical constraints of in-situ Argo observations. The dataset is designed for reuse in ocean state estimation, model validation, and climate-scale studies of eddy dynamics. By fusing SLA, geostrophic relative vorticity, and SSTA in a physics–data dual-driven segmentation framework, the production pipeline captures eddy signatures that are weak or non-closed in SLA alone, while preserving the geostrophic SLA–vorticity sign relationship. Rather than replacing existing altimetry atlases or sparse in-situ observations, the catalogue offers a higher-resolution, multimodal estimate that can reveal additional eddies in frontal and high-gradient regimes.

Independent leave-one-Argo-profile-out validation of the released product on 5,176 clear C/AC Argo profiles over 2010–2012 gives a hit rate of 87.1% and a type agreement of 92.1% following the production LOO polarity correction. On the identical profiles, the hit rate is higher than those reported for META4 (83.8%) and Faghmous et al. (2015) (76.0%), and the

https://doi.org/10.5194/essd-2026-670
Preprint. Discussion started: 5 October 2026
© Author(s) 2026. CC BY 4.0 License.

type agreement is higher than those of META4 (71.4%), Faghmous et al. (2015) (67.0%), and the CASEarth V3.0 SLA atlas (66.3%); CASEarth detects the largest fraction of Argo signals (93.1%) but has the lowest polarity agreement.

The dataset also reproduces physically meaningful climate signals. Application to ENSO reveals a robust negative correlation between eddy counts in the West Pacific–Philippines region and ONI in both PhyEddy-Net and META4, consistent with the eastward displacement of the warm pool and weakened trade-wind forcing during El Niño. By contrast, the classical east–west Pacific eddy seesaw—enhanced central–eastern Pacific activity during El Niño—is not supported by our analysis; correlations there are near zero in both products. Peru–Chile shows a weak but significant negative correlation in PhyEddy-Net that is absent or weaker in META4, suggesting that the released multimodal product detects additional ENSO-modulated eddies along the eastern boundary. These regional differences should be interpreted as complementary views of eddy–climate interactions rather than as evidence that either product is incorrect.

Future work will extend the product to the higher-resolution SWOT era, add a tracking module to produce long eddy trajectories, and incorporate additional satellite variables such as ocean colour and sea surface salinity to further constrain detection in physically complex regions.

Author contributions

Z.Q. and T.Z. designed the study and developed the PhyEddy-Net model. Z.X. and W.Z. performed the experiments and produced the dataset. W.Z. also contributed to data analysis, visualization, and figure preparation. C.W. contributed to manuscript preparation and data interpretation. All authors reviewed and approved the final manuscript.

Competing interests

The authors declare that they have no conflict of interest.

Acknowledgements

We thank AVISO+ and CMEMS for providing the altimetry products, NOAA for the OISST v2.1 product, and the International Argo Program for the in-situ profiles used for validation.

Data availability

The daily global PhyEddy-Net eddy detection dataset for 2010–2021 is available from Mendeley Data under the DOI https://doi.org/10.17632/rh6wtx3hyr.2 (Qiu et al., 2026), released under the CC BY 4.0 licence. The archive contains the eddy.zip catalogue (12 yearly CSV files, ~694 MB) and a README.txt file describing the data format, fields, units, and usage notes. The DOI resolves to a permanent landing page where the files can be browsed and downloaded.

https://doi.org/10.5194/essd-2026-670
Preprint. Discussion started: 5 October 2026
© Author(s) 2026. CC BY 4.0 License.

The original input datasets used to produce the catalogue are: the AVISO+ multi-mission SLA product distributed by CMEMS (DUACS DT2018; Taburet et al., 2019), available from https://marine.copernicus.eu; NOAA OISST v2.1 (Huang et al., 2021), available from https://psl.noaa.gov/data/gridded/data.noaa.oisst.v2.highres.html; the META4 eddy atlas (Pegliasco et al., 2022), available from https://www.aviso.altimetry.fr; and Argo data from the International Argo Program (https://argo.ucsd.edu). The Faghmous et al. (2015) global eddy dataset used for comparison is available from Dryad at https://doi.org/10.5061/dryad.gp40h.

References

Chaigneau, A., Le Texier, M., Eldin, G., Grados, C., Pizarro, O., 2011. Vertical structure of mesoscale eddies in the Eastern South Pacific Ocean: A composite analysis from altimetry and Argo profiling floats. J. Geophys. Res. Oceans 116, C11025, https://doi.org/10.1029/2011jc007134.

Chelton, D.B., Schlax, M.G., Samelson, R.M., 2011. Global observations of nonlinear mesoscale eddies. Prog. Oceanogr. 91, 167–216, https://doi.org/10.1016/j.pocean.2011.01.002.

Chen, G., Hou, Y., Chu, X., 2011. Mesoscale eddies in the South China Sea: Mean properties, spatiotemporal variability, and impact on thermohaline structure. J. Geophys. Res. Oceans 116, C06018, https://doi.org/10.1029/2010jc006716.

Faghmous, J.H., Frenger, I., Yao, Y., Warmka, R., Lindell, A., Kumar, V., 2015. A daily global mesoscale ocean eddy dataset from satellite altimetry. Sci. Data 2, 150028, https://doi.org/10.1038/sdata.2015.28.

Fan, R., Zhang, C., Zhang, S., Wang, Y., Yan, X., 2020. A multi-modal deep learning framework for oceanic mesoscale eddy detection based on satellite observations. Remote Sens. 12, 4135.

Ferrari, R., Wunsch, C., 2009. Ocean circulation kinetic energy: Reservoirs, sources, and sinks. Annu. Rev. Fluid Mech. 41, 253–282, https://doi.org/10.1146/annurev.fluid.40.111406.102139.

Fu, L.-L., Ubelmann, C., 2014. On the transition from profile altimeter to swath altimeter for observing global ocean surface topography. J. Atmos. Ocean. Technol. 31, 560–568, https://doi.org/10.1175/jtech-d-13-00109.1.

Gaube, P., Chelton, D.B., Samelson, R.M., Schlax, M.G., O'Neill, L.W., 2015. Satellite observations of mesoscale eddy-induced Ekman pumping. J. Phys. Oceanogr. 45, 104–132, https://doi.org/10.1175/jpo-d-14-0032.1.

Hang, R., Li, G., Xie, M., Wang, P., Ghamisi, P., 2022. Identifying oceanic eddy with an edge-enhanced multiscale convolutional network. IEEE J. Sel. Top. Appl. Earth Obs. Remote Sens. 15, 5453–5466, https://doi.org/10.1109/jstars.2022.3215696.

He, K., Zhang, X., Ren, S., Sun, J., 2016. Deep residual learning for image recognition. In: CVPR. IEEE, pp. 770–778, https://doi.org/10.1109/cvpr.2016.90.

Huang, B., Liu, C., Banzon, V., Freeman, E., Graham, G., Hankins, B., Smith, T., Zhang, H.-M., 2021. NOAA 0.25-degree daily optimum interpolation sea surface temperature (OISST), version 2.1. NOAA National Centers for Environmental Information. https://doi.org/10.25921/vsn3-md58.

https://doi.org/10.5194/essd-2026-670
Preprint. Discussion started: 5 October 2026
© Author(s) 2026. CC BY 4.0 License.

Karniadakis, G.E., Kevrekidis, I.G., Lu, L., Perdikaris, P., Wang, S., Yang, L., 2021. Physics-informed machine learning. Nat. Rev. Phys. 3, 422–440, https://doi.org/10.1038/s42254-021-00314-5.

Keppler, L., Cravatte, S., Chaigneau, A., Pegliasco, C., Gourdeau, L., Singh, A., 2018. Observed characteristics and vertical structure of mesoscale eddies in the southwest tropical Pacific. J. Geophys. Res. Oceans 123, 2731–2756, https://doi.org/10.1002/2017jc013712.

Lguensat, R., Sun, M., Fablet, R., Tandeo, P., Mason, E., Chen, G., 2018. EddyNet: A deep neural network for pixel-wise classification of oceanic eddies. J. Adv. Model. Earth Syst. 10, 406–428, https://doi.org/10.1029/2018MS001477.

Liu, T., Abernathey, R., 2023. A global Lagrangian eddy dataset based on satellite altimetry. Earth Syst. Sci. Data 15, 1765–1778. https://doi.org/10.5194/essd-15-1765-2023.

Ma, C., Gao, Z., Li, S., Li, S., Chen, G., 2022. SAR altimeter observations of mesoscale eddies in the South China Sea: A case study of super eddies. Remote Sens. 14, 1452.

Mason, E., Pascual, A., McWilliams, J.C., 2014. A new sea surface height–based code for oceanic mesoscale eddy tracking. J. Atmos. Ocean. Technol. 31, 1181–1188, https://doi.org/10.1175/jtech-d-14-00019.1.

McGillicuddy, D.J., 2016. Mechanisms of physical–biological–biogeochemical interaction at the oceanic mesoscale. Annu. Rev. Mar. Sci. 8, 125–159, https://doi.org/10.1146/annurev-marine-010814-015606.

Morrow, R., Fu, L.-L., Ardhuin, F., Benkiran, M., Chapron, B., Cosme, E., d'Ovidio, F., Farrar, J.T., Gille, S.T., Lapeyre, G., Le Traon, P.-Y., Pascual, A., Ponte, A., Qiu, B., Rascle, N., Ubelmann, C., Wang, J., Zaron, E.D., 2019. Global observations of fine-scale ocean surface topography with the Surface Water and Ocean Topography (SWOT) mission. Surv. Geophys. 40, 809–825, https://doi.org/10.1007/s10712-019-09536-9.

Moschos, E., Stegner, A., Le Vu, B., Schwander, O., 2023. Deep learning for oceanic eddy detection from satellite altimetry. Front. Mar. Sci. 10, 1150839, https://doi.org/10.3389/fmars.2023.1150839.

Nencioli, F., Dong, C., Dickey, T., Washburn, L., McWilliams, J.C., 2010. A vector geometry–based eddy detection algorithm and its application to a high-resolution numerical model product and high-frequency radar surface velocities in the Southern California Bight. J. Atmos. Ocean. Technol. 27, 564–579, https://doi.org/10.1175/2009jtecho725.1.

Pegliasco, C., De Boisséson, E., Morrow, R., 2022. META3.1exp: A new global mesoscale eddy trajectory atlas from altimetry. SEANOE. https://doi.org/10.17882/87168.

Qiu, B., Chen, S., Klein, P., Wang, J., Torres, H., Fu, L.-L., Menemenlis, D., 2023. Reconstructing upper-ocean vertical velocity field from sea surface height in the presence of unbalanced motion. J. Phys. Oceanogr. 53, 2339–2358, https://doi.org/10.1175/jpo-d-19-0172.1.

Qiu, Z., Zong, T., Xia, Z., Zhou, W., Wang, C., 2026. A daily global mesoscale eddy detection dataset at 0.125° spatial resolution for 2010–2021 generated by PhyEddy-Net. Mendeley Data V2. https://doi.org/10.17632/rh6wtx3hyr.2.

Ronneberger, O., Fischer, P., Brox, T., 2015. U-Net: Convolutional networks for biomedical image segmentation. In: MICCAI. Springer, pp. 234–241, https://doi.org/10.1007/978-3-319-24574-4_28.

https://doi.org/10.5194/essd-2026-670
Preprint. Discussion started: 5 October 2026
© Author(s) 2026. CC BY 4.0 License.

Roy, A.G., Navab, N., Wachinger, C., 2018. Concurrent spatial and channel "squeeze & excitation" in fully convolutional networks. In: MICCAI. Springer, pp. 421–429, https://doi.org/10.1007/978-3-030-00928-1_48.

Santana, O.J., Hernandez-Sosa, D., Smith, R.N., 2022. Oceanic mesoscale eddy detection and convolutional neural networks. Remote Sens. 14, 4179.

Taburet, G., Sanchez-Roman, A., Ballarotta, M., Pujol, M.-I., Legeais, J.-F., Fournier, F., Faugere, Y., Dibarboure, G., 2019. DUACS DT2018: 25 years of reprocessed sea level altimetry products. Ocean Sci. 15, 1207–1224, https://doi.org/10.5194/os-15-1207-2019.

Wang, Y., Chen, G., Li, X., 2021. Attention-enhanced deep learning for oceanic mesoscale eddy detection from satellite altimetry. Remote Sens. 13, 1906.

Yakubovskiy, P., 2020. Segmentation models pytorch. GitHub repository. https://github.com/qubvel/segmentation_models.pytorch.

Zhang, Z., Wang, W., Qiu, B., 2014. Oceanic mass transport by mesoscale eddies. Science 345, 322–324, https://doi.org/10.1126/science.1252418.

Zhao, Y., Fan, Z., Li, H., Sun, C., Ji, Y., 2023. Symmetric net: End-to-end mesoscale eddy detection with multi-modal data fusion. Front. Mar. Sci. 10, 1174818, https://doi.org/10.3389/fmars.2023.1174818.